Soft Matter

Spatiotemporal control of micromechanics and microstructure in acoustically-responsive scaffolds using acoustic droplet vaporization

Journal:	*Soft Matter*
Manuscript ID	SM-ART-04-2020-000753.R1
Article Type:	Paper
Date Submitted by the Author:	12-Jun-2020
Complete List of Authors:	Aliabouzar, Mitra; University of Michigan, Radiology Davidson, Christopher; University of Michigan, Biomedical Engineering Wang, William; University of Michigan Department of Biomedical Engineering, Biomedical Engineering Kripfgans, Oliver; University of Michigan, Radiology Franceschi, Renny; University of Michigan Putnam, Andrew; University of Michigan, Biomedical Engineering Fowlkes, J.; University of Michigan, Baker, Brendon; University of Michigan, Biomedical Engineering; University of Michigan Fabiilli, Mario; University of Michigan, Ann Arbor, USA, Radiology

Spatiotemporal control of micromechanics and microstructure in acoustically-responsive scaffolds using acoustic droplet vaporization

Mitra Aliabouzar[1], Christopher D. Davidson[2], William Y. Wang[2], Oliver D. Kripfgans[1,2,3], Renny T. Franceschi[2,4], Andrew J. Putnam[2], J. Brian Fowlkes[1,2,3], Brendon M. Baker[2], and Mario L. Fabiilli[1,2,3]

[1]Department of Radiology, University of Michigan, Ann Arbor, MI, USA

[2]Department of Biomedical Engineering, University of Michigan, Ann Arbor, MI USA

[3]Applied Physics Program, University of Michigan, Ann Arbor, MI USA

[4]School of Dentistry, University of Michigan, Ann Arbor, MI USA

Corresponding Author:

Mario L. Fabiilli, Ph.D.

University of Michigan

3226A Medical Sciences Building I

1301 Catherine Street

Ann Arbor, MI 48109-5667

Phone: 734-647-9326

E-mail: mfabiill@umich.edu

Abstract

Acoustically-responsive scaffolds (ARSs), which are composite fibrin hydrogels, have been used to deliver regenerative molecules. ARSs respond to ultrasound in an on-demand, spatiotemporally-controlled manner via a mechanism termed acoustic droplet vaporization (ADV). Here, we study the ADV-induced, time-dependent micromechanical and microstructural changes to the fibrin matrix in ARSs using confocal fluorescence microscopy as well as atomic force microscopy. ARSs, containing phase-shift double emulsion (PSDE, mean diameter: 6.3 μm), were exposed to focused ultrasound to generate ADV – the phase transitioning of the PSDE into gas bubbles. As a result of ADV-induced mechanical strain, localized restructuring of fibrin occurred at the bubble-fibrin interface, leading to formation of locally denser regions. ADV-generated bubbles significantly reduced fibrin pore size and quantity within the ARS. Two types of ADV-generated bubble responses were observed in ARSs: super-shelled spherical bubbles, with a growth rate of 31 μm/day in diameter, as well as fluid-filled macropores, possibly as a result of acoustically-driven microjetting. Due to the strain stiffening behavior of fibrin, ADV induced a 4-fold increase in stiffness in regions of the ARS proximal to the ADV-generated bubble versus distal regions. These results highlight that the mechanical and structural microenvironment within an ARS can be spatiotemporally modulated using ultrasound, which could be used to control cellular processes and further the understanding of ADV-triggered drug delivery for regenerative applications.

Keywords: acoustic droplet vaporization, phase-shift emulsion, micromechanics, atomic force microscopy, fibrin gels, microjetting, confocal microscopy, ultrasound

1 Introduction

Conventional hydrogels used for tissue engineering possess uniform mechanical properties, such as stiffness, and microstructural features, such as microporosity [1]. Therefore, after fabrication or implantation, these *a priori* parameters cannot be dynamically changed externally. Unlike conventional hydrogels, the extracellular matrix (ECM), which is the major component of the cellular microenvironment, is a highly dynamic structure both spatially and temporally based on homeostatic and pathological events. Cells respond to biochemical and biophysical cues within native (i.e., ECM) and surrogate (i.e., hydrogel) microenvironments. Yet, the impact of these cues, especially biophysical signals, on cell behaviors (e.g., migration, proliferation) has not been fully elucidated. This has hindered the translation of many regenerative therapies. Thus, designing hydrogels with mechanical and structural properties that can be tuned non-invasively and spatiotemporally, via an externally-controlled mechanism, would be beneficial in understanding the role of biophysical cues on cells, which ultimately could be used in directing regenerative processes.

Due to its temporal and spatial specificity, along with its non-invasive and on-demand characteristics, ultrasound (US) is highly desirable for therapeutic applications [2, 3]. One application of focused US is the phase transition of volatile perfluorocarbon (PFC) droplets into gas bubbles in a process termed acoustic droplet vaporization (ADV) [4]. The vaporization of the PFC liquid using acoustic waves occurs above a threshold value of the rarefactional pressure (i.e., the ADV threshold) at which the phase transition becomes energetically favorable. Upon ADV, the PFC phase undergoes a volumetric expansion, which is approximately 125-fold in water for sufficiently sized droplets [5, 6]. The presence of a viscoelastic medium such as a surrounding hydrogel reduces this expansion factor [7]. The ultimate fate of the ADV-generated bubbles (i.e., re-condenstation,

stable oscillation, or inertial cavitation) is determined by acoustic parameters such as excitation pressure and oscillation period, as well as medium rheology such as elasticity [8, 9]. In fluids such as water, inertial cavitation (IC) occurs when the bubble grows to at least twice its original diameter, followed by a violent collapse driven by the inertia of the fluid. We previously showed that ADV occurred at lower rarefactional pressures than IC, indicating that phase transition precedes IC [10, 11].

ADV can be spatiotemporally and non-invasively controlled using focused US pulses. We have utilized ADV to control release of therapeutic agents encapsulated in phase-shift double emulsions (PSDEs) with a structure of water-in-PFC-in-water (W_1/PFC/W_2). The deliverable payload is contained within the innermost water phase (i.e., W_1). US can disrupt the morphology of the PSDEs by phase-transitioning the PFC phase, thereby releasing the payload. These PSDEs can be incorporated into implantable fibrin scaffolds to produce a composite hydrogel, termed an acoustically-responsive scaffold (ARS)[12]. ARSs have been used in conjunction with ADV in both *in vitro* and *in vivo* studies to control single and sequential delivery of fluorescently-labeled dextran as well as regenerative growth factors (e.g., basic fibroblast growth factor (bFGF), platelet-derived growth factor (PDGF)) as shown previously [13-17].

Although several studies have investigated the impact of bulk medium properties (e.g., elasticity and viscosity) on the ADV phenomenon (i.e., the ADV threshold)[10, 18, 19], the effect of ADV on the surrounding medium has been understudied. Changes in the mechanical properties of ARSs post-ADV can affect the kinetics of payload release as well as fibrin degradation. We previously showed that the presence of ADV-generated bubbles lowered the degradation rate of ARSs in an *in vitro* study, either due to hindered diffusivity or strain-induced stiffening in fibrin [13]. Using dynamic shear testing, a 300% increase in shear stiffness for an ARS post-ADV was

reported by Fabiilli et al[12]. However, these studies were conducted using bulk characterization methods which are insensitive to microscale mechanical heterogeneities. A better understanding of ADV-induced micromechanical changes in ARSs could improve their design and performance as well as broaden their application beyond drug delivery.

Here, confocal fluorescence imaging was used to visualize and quantify ADV-induced changes in the microstructure of ARSs, such as pore size distribution, over time. Growth dynamics and morphology of different ADV-generated features, such as spherical bubbles as well as asymmetrically collapsed bubbles, were examined. Additionally, we used atomic force microscopy (AFM) to study the spatial heterogeneity of the micromechanical properties of ARSs before and after ADV. Ultimately, elucidating the mechanical and structural microenvironments within the ARS could be used to control mechanically-induced cellular processes and further the understanding of ADV-triggered drug delivery for regeneration.

2 Materials and Methods

2.1 Preparation and characterization of PSDE

The in-house manufacture of PSDE with a $W_1/PFC/W_2$ structure has been described previously[15]. Perfluorohexane (C_6F_{14}, CAS# 355-42-0, bulk boiling point: 56°C, Strem Chemicals) was used as the PFC phase. A fluorosurfactant copolymer, synthesized using a 2:1 molar ratio of Krytox 157 FSH (CAS# 51798-33-5, DuPont, Wilmington, DE, USA) and poly(ethylene glycol) bis(amine) (MW: 1000 g/mol, CAS# 24991-53-5, Alfa Aesar, Ward Hill, MA, USA), was dissolved at 2% (w/w) in PFC. The PFC solution was combined at 2:1 (v/v) with a W_1 phase containing 1.66 mg/mL Alexa Fluor 488-labeled dextran (AF_{488}, MW: 10,000 Da, Life Technologies, Grand Island, NY, USA) in phosphate buffered saline (PBS, Life Technologies), and then sonicated (Q55 with CL-188 immersion probe, QSonica, LLC, Newton, CT, USA) for

30 seconds while on ice. To produce PSDEs, the primary emulsion (i.e., W_1/PFC) and W_2 phase, which was 50 mg/mL Pluronic F68 (CAS# 9003-11-6, Sigma-Aldrich, St. Louis, MO, USA) in PBS, were pumped at 1 μL/min and 10 μL/min, respectively, through a quartz microfluidic chip (Cat# 3200146, junction: 14 μm × 17 μm, Dolomite, Royston, United Kingdom), as shown in Fig. 1(A). Using a Coulter Counter (Multisizer 4, Beckman Coulter, Brea, CA, USA) with a 50 μm aperture tube, the average diameter, coefficient of variation, and concentration of PSDE were 6.3 ± 0.06 μm, 16.2 ± 0.3%, and (7.1 ± 1.1) × 10^9 particles /mL, respectively.

2.2 Preparation of ARSs

ARSs were prepared by first dissolving bovine fibrinogen (Sigma-Aldrich) in FluoroBrite Dulbecco's modified Eagle's medium (DMEM, Life Technologies) either at 20 mg/mL (for AFM studies) or 5 mg/mL (for confocal studies) clottable protein while under gentle vortex mixing for 30 seconds. A lower fibrinogen concentration was chosen for confocal studies for better visualization of microstructural changes in fibrin since the mesh size correlates indirectly with fibrinogen concentration [20]. The fibrinogen solution and additional DMEM were degassed separately in a vacuum chamber (Isotemp vacuum oven, Model 282A, Fisher Scientific, Dubuque, IA, USA) at ~6 kPa for 60 minutes to minimize the amount of dissolved gas, which could act as cavitation nuclei. ARSs were made by combining the prepared fibrinogen, DMEM, 0.005% (v/v) PSDE, bovine lung aprotinin (Sigma-Aldrich), and bovine thrombin (Thrombin-JMI, King Pharmaceuticals, Bristol, TN, USA). The final concentrations of fibrinogen, aprotinin, and bovine thrombin in the ARSs were 10 mg/mL (2.5 mg/mL for confocal studies), 0.05 U/mL, and 2 U/mL, respectively. To enable visualization of the matrix, 39 μg/mL Alexa Fluor 647-labeled fibrinogen ($fibrinogen_{647}$) was added to each ARS prior to polymerization. Each well in the BioFlex plate was coated with 1% (w/v) solution of bovine serum albumin (CAS# 9048-46-8, Sigma-Aldrich) in PBS

(for ~30 minutes) prior to polymerization of the ARSs to facilitate removal of the scaffolds. Aliquots (volume = 0.5 mL, height (h) ~3mm) of the ARS mixture were added to each well of 24-well BioFlex plates (total well diameter: 15 mm, membrane thickness: 0.2 mm, and total height: 15 mm, Flexcell International, Burlington, NC, USA), and allowed to polymerize for 15 minutes at room temperature (Fig. 1(B)).

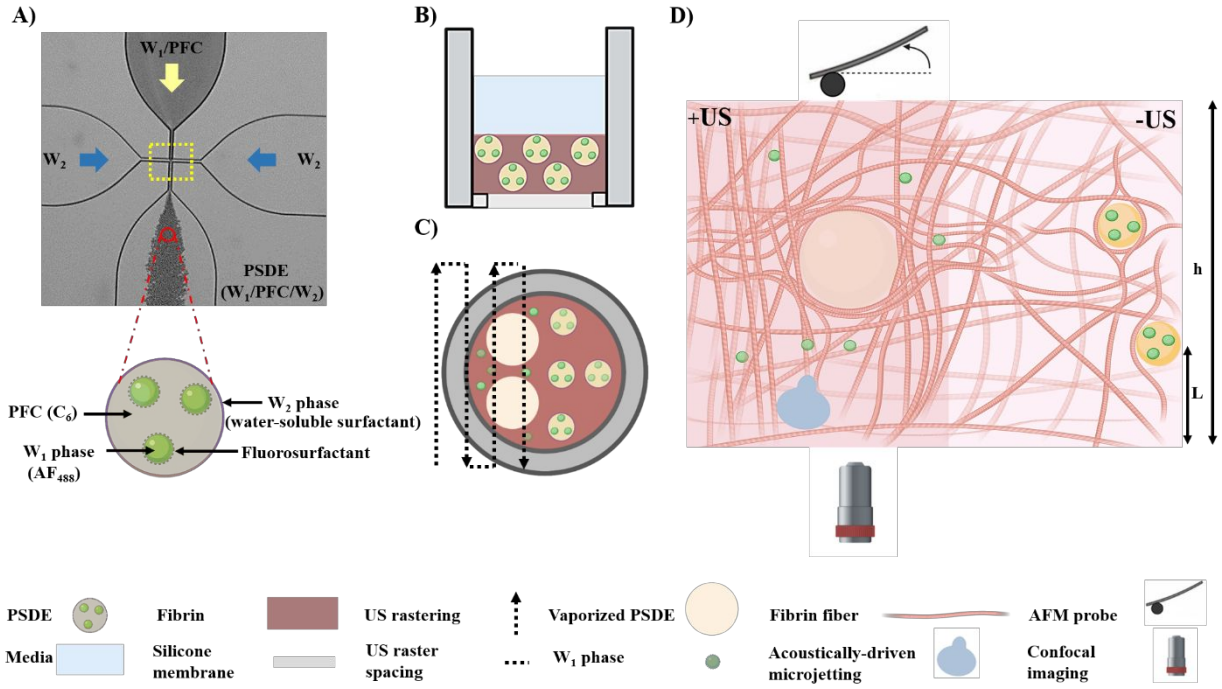

Figure 1. (A) An image of the microfluidic chip showing the flow focusing geometry of the junction (14 µm × 17 µm, highlighted in a yellow dotted box). The phase-shift double emulsion (PSDE) was generated by pumping the inner (W_1/PFC) and outer (W_2) fluids at 1 and 10 µL/min, respectively. The enlarged feature displays a schematic of a PSDE loaded with Alexa Fluor 488-labeled dextran (AF_{488}). (B) An acoustically-responsive scaffold (ARS) containing perfluorohexane (C_6)-AF_{488} PSDE in a BioFlex plate. The plate was positioned on the surface of a water tank and ultrasound (US) was applied through the silastic well bottom. (C) The top-down view of an ARS, US raster pattern, and lateral raster spacing are shown. (D) A schematic displaying an ARS, with the left half exposed to US, and depicting the microstructural changes induced by acoustic droplet vaporization (ADV). The ADV-induced features, spherical bubbles and asymmetrically collapsed bubbles, as well as the resulting microstructural changes in fibrin were studied using atomic force microscopy (AFM) and confocal imaging. L is the distance of the centroid of the droplet from the bottom of the gel, and h is the total height of an ARS. Figures were created with BioRender.com.

2.3 US exposure setup and parameters

All US experiments were conducted in a water tank (30 cm × 60 cm × 30 cm) filled with degassed (12-22% O_2 saturation, where 100% O_2 means equilibrium with air), deionized water at 37°C. A calibrated, focused transducer (2.5 MHz, H-108, f-number = 0.83, radius of curvature = 50 mm, Sonic Concepts Inc., Bothell, WA, USA) was used to generate ADV within the ARSs. Pulsed waveforms (2.5 MHz, pulse duration: 5.4 μs; pulse repetition frequency (PRF): 100 Hz; duty cycle: 0.05%) were generated by a function generator (33500B, Agilent Technologies, Santa Clara, CA, USA) and amplified by a gated radiofrequency (RF) amplifier (68 dB gain, GA-2500A Ritec Inc., Warwick, RI, USA). The generated amplified signals were viewed and monitored in real-time on an oscilloscope (HDO4034, Teledyne LeCroy, Chestnut Ridge, NY, USA). To reduce the impedance mismatch between the transducer and the amplifier, a matching circuit (H108_3 MN, Sonic Concepts) was used. The transducer was calibrated in free field at the focus in the range of 1.5-8 MPa peak rarefactional pressure (2-40 MPa peak compressional pressure) at the fundamental frequency (i.e., 2.5 MHz), using an in-house fiber optic hydrophone (sensitivity: 16.6 mV/MPa) with a fiber diameter of 105 μm [21].

Experiments were conducted by placing the BioFlex plate containing the ARSs in the water tank such that only the bottom of the plate was in contact with water. ARSs were kept in the water tank at 37°C for 15 minutes (verified by calculation of thermal boundary layer thickness) prior to ADV studies to reach thermal equilibrium. The transducer was positioned under the plate and connected to a three-axis positioning system controlled by MATLAB (The MathWorks, Natick, MA, USA). The transducer was continuously rastered at 5 mm/s with a lateral spacing of 0.8 mm (Fig. 1(C)). To localize the transducer axially with respect to the ARSs, a pulse echo technique was utilized whereby the transducer was driven by a pulser-receiver (5077PR, Olympus, Center

Valley, PA, US) at low pressures to avoid ADV. The axial focus of the transducer was positioned and maximized with respect to reflections from the well bottom (silicone elastomer membrane with a characteristic impedance (Z) of ~1.2 MRayl) as well as the overlying media-air interface (Z ~0.43 MRayl) [22]. In addition to minimized reflections from the well bottom (due to the low acoustic impedance mismatch), the measured US attenuation of this membrane (thickness ~0.2 mm) was measured to be 0.7 ± 0.2 dB/MHz/cm [23], indicating insignificant interference with the sound field at this frequency. Beam characterization of the transducer at the focus, using the hydrophone, yielded an axial length and lateral width at full width half maximum (FWHM) of 3.9 ± 0.1 mm (theoretical value: 3.28 mm) and 0.7 ± 0.1 mm (theoretical value: 0.51 mm), respectively, at 2.5 MHz [13]. Since h ~3 mm, a single z-plane of exposure was used throughout the studies by placing the focus of the transducer at mid-height in the ARSs. Unless otherwise noted, all acoustic pressures are listed as peak rarefactional pressure (P_r). In this study, all the US experiments were conducted at P_r = 8 MPa (peak compressional pressure = 40 MPa), which was suprathreshold for both ADV (2.2 ± 0.2 MPa) and IC (3.9 ± 0.2 MPa) thresholds at 2.5 MHz [13, 24]. Control ARSs (i.e., ARS (-US)) were exposed to sham US.

For experiments involving exposing the ARSs to overpressure, ARSs were removed from the 24-well plates post-ADV and placed separately in a 10 mL Luer-Lock tip air-filled syringe connected to a differential pressure manometer (35 kPa, Extech, Melrose, Ma, USA) for one minute. ARSs were imaged following compression.

2.4 Confocal imaging

For confocal imaging, ARSs and fibrin-only gels (h ~3 mm) were placed in a cell chamber (Attofluor, A7816, Thermo Fisher Scientific, Waltham, MA, USA). Scaffolds were imaged with a laser scanning confocal microscope with an environmental chamber (37°C) (LSM800, Zeiss,

Pleasanton, CA, USA; C2+, Nikon, Melville, NY, USA) using 10x, 20x, and 40x objectives. To study interactions of the ADV-generated bubbles with fibrin at the bubble-fibrin interface over multiple timepoints, the laser power was set to the lowest non-zero setting (0.2 %) to minimize saturation. To investigate the effect of bubble growth on the fibrin microstructure, a higher laser setting (1%) was chosen for better visualization of the matrix. For time dependent qualitative and quantitative analyses, ARSs were imaged 1-hour (1h) through 4 days (4d) post-ADV. ARSs post-ADV were kept in a cell culture incubator (37°C, 5% carbon dioxide) over the timepoints studied here.

2.4.1 Image analysis

Intensity measurements were performed on selected confocal images using ZEN lite software (Zeiss). To determine a decay constant for the intensity profiles, the distance from the bubble-fibrin interface was discretized into multiple regions of interest (ROIs) and the data were fit to a one phase decay model as follows:

$$y = (y_0 - y_{min})\, e^{(-K * x)} + y_{min}$$

where y_0 is the maximum intensity, y_{min} is the intensity at infinite distance, x is the position of the ROI from the interface, and K is the rate constant ($(ROI)^{-1}$).

The FWHM thickness of intensity-distance profiles was calculated by excluding pixels within the saturated region and fitting the intensity profiles with a Gaussian model as follows:

$$y = \sum_{i=1}^{n} a_i e^{\left[-\left(\frac{x-b_i}{c_i}\right)^2\right]}$$

where a is the amplitude, b is the mean, c is related to the peak width, and n is the number of peaks to fit.

To calculate pore size distribution within fibrin-only gels as well as ARSs post-ADV, the resulting scaling factor (μm/pixel) from the confocal images was used with a custom MATLAB program. Details of implemented morphological and transform functions for image processing can be found elsewhere [25, 26].

2.5 AFM sample preparation and measurements

ARSs (h ~ 1.5 mm) were immobilized on a 35 mm dish (PN#353001, Fisher Scientific) using high-vacuum silicone grease (SKU# Z273554, Sigma-Aldrich). Force-distance (F-d) curves were acquired on fibrin-only gels, ARSs (-US), and ARSs (+US) over predetermined time points using the Nanosurf FlexBio AFM (Liestal, Switzerland) mounted on an inverted optical microscope (Observer3, Zeiss). The samples were mechanically interrogated using a silicon nitride cantilever (nominal spring constant: 0.046 N/m, HYDRA6V-200NG-TL-10, AppNano, Mountain View, CA, USA) and a spherical glass bead (radius: 3 μm, 14910530, Corpuscular Inc, Cold Spring, NY, USA) glued to the end of the cantilever. All AFM experiments were conducted in contact mode. Prior to measurements, the cantilever spring constant was determined automatically using the built-in thermal tuning method. Laser beam deflection sensitivity was calibrated on the same substrate before the measurements. Cantilever speed was kept constant (~2 μm/s) for all the measurements. Note that effects of scanning speed (0.5 to 3 μm/s) and cantilever spring constant (0.03 to 0.6 N/m) caused no significant variations in the AFM measurements [27, 28].

F-d curves were converted to force-indentation (F-δ) curves, according to Hooke's law, using open source software, AtomicJ (http://sourceforge.net/projects/jrobust). The loading part of

the curve was used for data analysis. Compressive Young's modulus was approximated from the F-δ curve, assuming a linear elastic material following Hertz model [29, 30]:

$$F(\delta) = \frac{4E\sqrt{R}}{3(1-v^2)}\delta^{3/2}$$

where R is the radius of the incompressible spherical probe pushed down with a force (F) on a flat, elastic surface, with Young's modulus of E resulting in indentation of the surface, δ. The Poisson ratio (ν) can be determined from the volume changed during indentation and is usually assumed to be 0.5 for cells and most hydrogels [31, 32]. All AFM measurements were performed in liquid DMEM at room temperature. ARSs post-ADV were kept in a cell culture incubator (37°C, 5% carbon dioxide) over the timepoints studied here.

2.6 Statistical analyses

Statistical analyses were performed using GraphPad Prism software (GraphPad Software, Inc., La Jolla, CA, USA). The Shapiro-Wilk test was used to test normality of data. For those failing the normality test, data are presented in the format S [S_L, S_U] where S is median, S_L is the lower quartile and S_U is the upper quartile. The rest of the data are expressed as the mean ± standard deviation. The number of independent replicates is listed in the caption for each figure. Significant differences between groups were determined using *t*-tests as well as one-way ANOVA followed by Tukey's multiple comparisons test, with a significance level of 0.05.

3 Results and discussion

3.1 Confocal microscopy characterization

3.1.1 Time-dependent fluorescence intensity measurements in ARSs pre- and post-ADV

Figure 2(A) shows a confocal microscopy image of an ARS containing a PSDE (∅: 5.3 μm) (i.e., before ADV). The W_1 phase within the PSDE is displayed in green due to the presence of AF_{488} while the fibrin matrix, surrounding the PSDE, is shown in red due to the inclusion of $fibrinogen_{647}$. Fibrin-only gels, without PSDE, exhibited a similar homogeneous distribution of $fibrinogen_{647}$ (not shown). The resultant ADV-generated bubble (∅ ~40 μm) was imaged 1h post ADV (Fig. 2(B)). The volumetric expansion of the PFC phase during ADV, successive expansion and contraction cycles post-ADV, and further growth of the generated bubbles due to in-gassing over the timepoints studied here induced repetitive localized strain to the fibrin gel, resulting in local microstructural rearrangement of the fibrin network. If the forcing period (τ), which is the inverse of frequency (□), is much shorter than the stress relaxation time of fibrin (ζ), strain continues to build up cycle after cycle of oscillation. ζ is given by the ratio of viscosity (~50 mPa•s) to shear modulus (~0.02 kPa) of the material (fibrin) [12, 33, 34]. Here, ζ is ~ 3 ms and τ ~ 0.4 μs. A strain-dependent stress relaxation times of 1-300 s has been reported for collagen and fibrin gels under creep studies [35]. As shown in Fig. 2(B), consolidation of the fibrin at the bubble-fibrin interface, likely due to the ADV-induced mechanical strain, resulted in an elevated fluorescence intensity in those regions. The corresponding line intensity measurements for AF_{488} and $fibrinogen_{647}$ signals were performed on ARSs before and after ADV at the lowest confocal laser power setting to minimize saturation (Fig. S1).

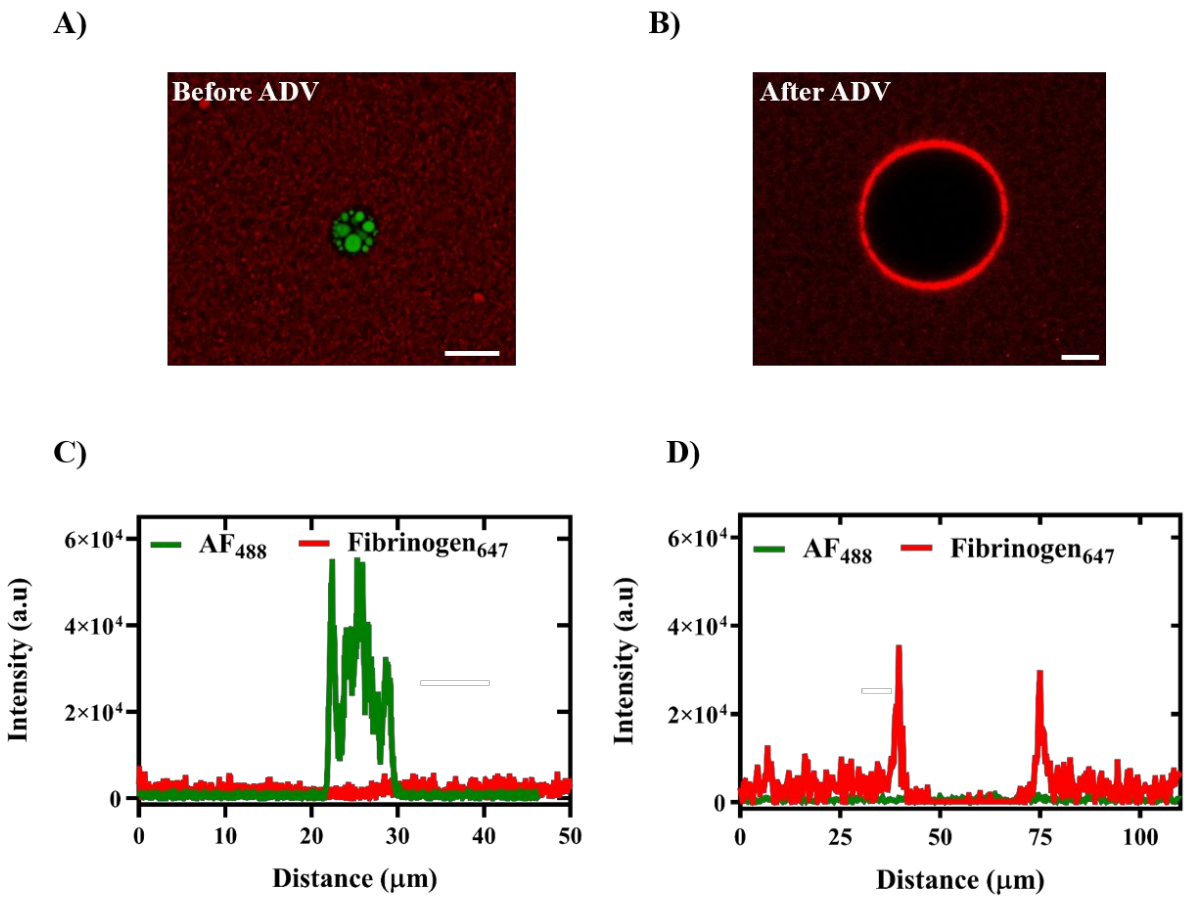

Figure 2. Confocal microscopy revealed local compaction of fibrin surrounding the bubbles generated by acoustic droplet vaporization (ADV). Images of acoustically-responsive scaffolds (ARSs) (A) before and (B) 1-hour after ADV. The fibrin matrix contained Alexa Flour 647-labeled fibrinogen (fibrinogen$_{647}$, shown in red) while the phase-shift double emulsion contained Alexa Flour 488-labeled dextran (AF$_{488}$, shown in green). Line intensity measurements of AF$_{488}$ and fibrinogen$_{647}$ (C) before and (D) 1-hour after ADV. Scale bar:10 μm.

As seen by comparing Figs. 2(C) & (D), AF$_{488}$ intensity decreased significantly to almost background noise 1h post ADV, indicating complete release of the payload, while fibrinogen$_{647}$ intensity increased significantly at the interface of the ADV-generated bubble and fibrin, indicating formation of locally denser regions. Since the diffusion coefficient of AF$_{488}$ is ~10^{-4} mm^2/s at room temperature in a 2.5 mg/mL fibrin gel [36], the fluorescent molecules would have diffused ~0.5 mm within the ARS 1h-post ADV. Therefore, AF$_{488}$ would not be within the

optical field of view around the bubble 1h-post ADV. However, parameters such as medium rheology and volume faction of bubbles could impact the diffusion time scale[13, 14].

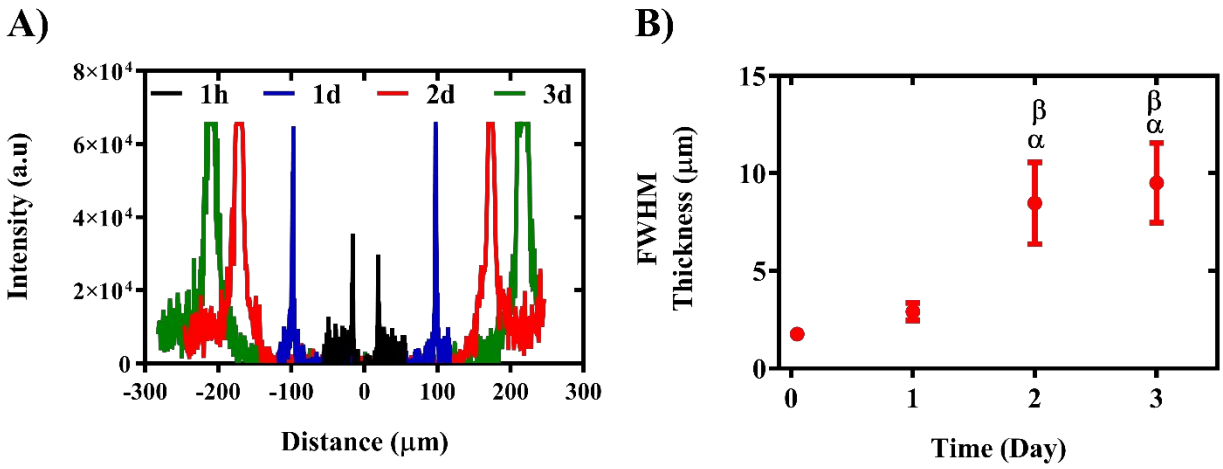

Figure 3. Longitudinal growth of bubbles, generated via acoustic droplet vaporization (ADV), significantly increased fibrin compaction at the fibrin-bubble interface in acoustically-responsive scaffolds (ARSs). (A) Line intensity measurements of Alexa Flour 647-labeled fibrinogen (fibrinogen$_{647}$) in ARSs 1-hour (1h), 1-day (1d), 2 days (2d), and 3 days (3d) post-ADV. Time-dependent intensity measurements were performed on confocal images containing a single ADV-generated bubble (similar to Fig. S1(B)).(B) Gaussian fitting was performed on the intensity-distance data from (A) to calculate the full width at half maximum (FWHM) thickness of the high intensity region over time (n=5). Statistically significant differences ($p < 0.05$) are denoted as follows: α: vs. 1h; β: vs. 1d.

Similarly, we quantified the change in the fluorescence intensity as well as the FWHM thickness of the consolidated region as the ADV-generated bubble grew due to static diffusion (i.e., in the absence of a changing pressure field) over time (Fig. 3). The fluorescence intensity at the interface increased ~18.5-fold 1h post-ADV compared to pre-ADV levels. Additionally, the intensity increased ~2-fold as the ADV-generated bubble grew from ~44 μm 1h post-ADV into ~163 μm on day 1 (Fig. 3(A)). The fluorescence intensity saturated on 2d and 3d. FWHM thickness of the high intensity region, fit to a Gaussian function (section 2.4.1), increased

significantly over time as shown in Fig. 3(B), indicating more consolidation of fibers around the growing bubble.

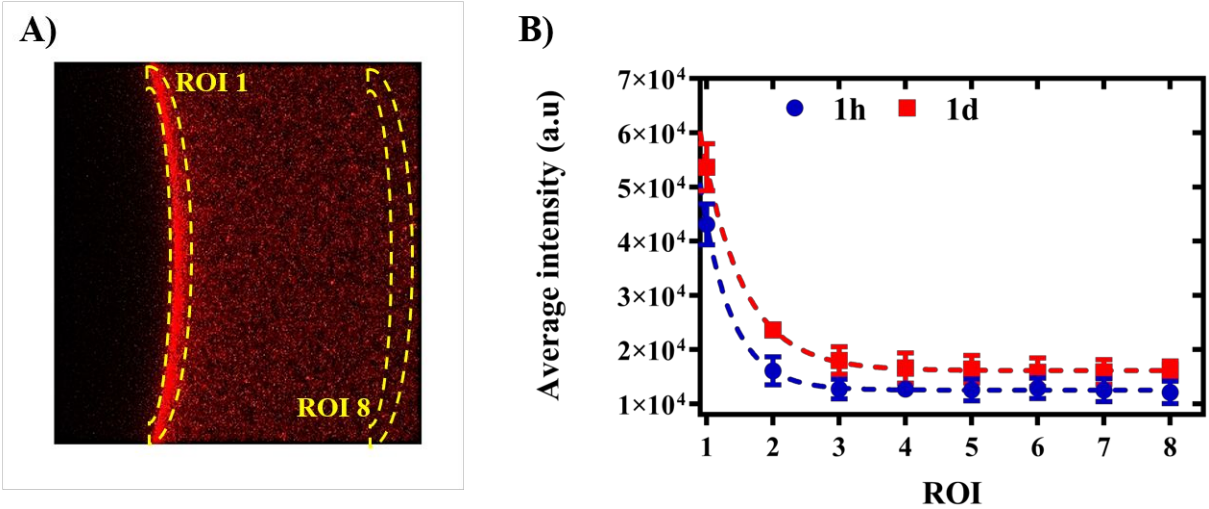

Figure 4. Effect of acoustic droplet vaporization (ADV) on fibrin microstructure in different regions of interest (ROIs) from the interface of the ADV-generated bubble. (A) Different ROIs (outlined in yellow dashed lines), each having a length of 3.5 µm, were defined on the confocal image (79.5 µm by 79.5 µm) of an acoustically- responsive scaffold containing a single ADV-generated bubble. The image was taken using a 40x objective with an optical zoom factor of 2x. (B) Intensity measurements of Alexa Flour 647-labeled fibrinogen in 8 ROIs at 1-hour (1h) and 1 day (1d) post-ADV (n=3).

To elucidate the impact of the ADV-generated bubbles on fibrin microstructure, the confocal image was segmented into 8 ROIs, each having a length of ~3.5 µm, as displayed in Fig. 4(A). Fibrinogen$_{647}$ intensity decreased exponentially from the ROI proximal to the bubble-fibrin interface (ROI 1) to the most distal (ROI 8). The decay constant (K, ROI^{-1}), fit to a one phase decay model, was 2.2 and 1.6 after 1h and 1d, respectively (Fig. 4(B)). The lower decay on 1d compared to 1h was consistent with the statistical analysis showing that the significant increase in intensity was one ROI (i.e., ROI 1) after 1h and two ROIs (i.e., ROI 1 & ROI 2) on 1d before reaching a plateau. This indicates that the region of influence by the growing bubble increases over time.

To further examine the effect of ADV on the fibrin matrix, the pore size distribution was calculated for fibrin-only (-US) (Fig. 5(A)) as well as an ARS post ADV (Fig. 5(D)). Pore size analysis was implemented on the binary images of fibrin-only (Fig. 5(B)) and an ARS post ADV (Fig. 5(E)). The corresponding pore size distribution of a fibrin-only gel is presented in Fig. 5(C), showing an average pore size of 1.2 ± 0.5 μm, which is in agreement with the reported average pore size of 1.69 ± 0.33 μm for fibrin (3.3 mg/mL fibrinogen) using ImageJ analysis [37]. Furthermore, the presence of an ADV-generated bubble affected both the size and number of pores locally as demonstrated in Fig. 5(F).

Unlike rubber-like elastomers or flexible polymers, fibrin is known to exhibit strain stiffening [38, 39]. Previous studies reported densification of the fibrin network [40] and increases in elastic [41] as well as loss [35] moduli in response to applied mechanical strain. Localized densification of the fiber around an expanding air bubble in a microfibrous cellulose network, visualized by particle image velocimetry, correlated inversely with fiber concentration, likely due to more available space for fiber rearrangement in sparser networks [42]. At a cellular level, cells embedded in three-dimensional matrices (such as fibrin and collagen) exerted traction forces (typically in the nN range) on their surroundings, driving the gel into a nonlinear, stress-stiffened regime [43-45]. In addition, cellular traction forces resulted in a highly condensed fibrin network in a radial distance of ~30 μm after overnight incubation [46].

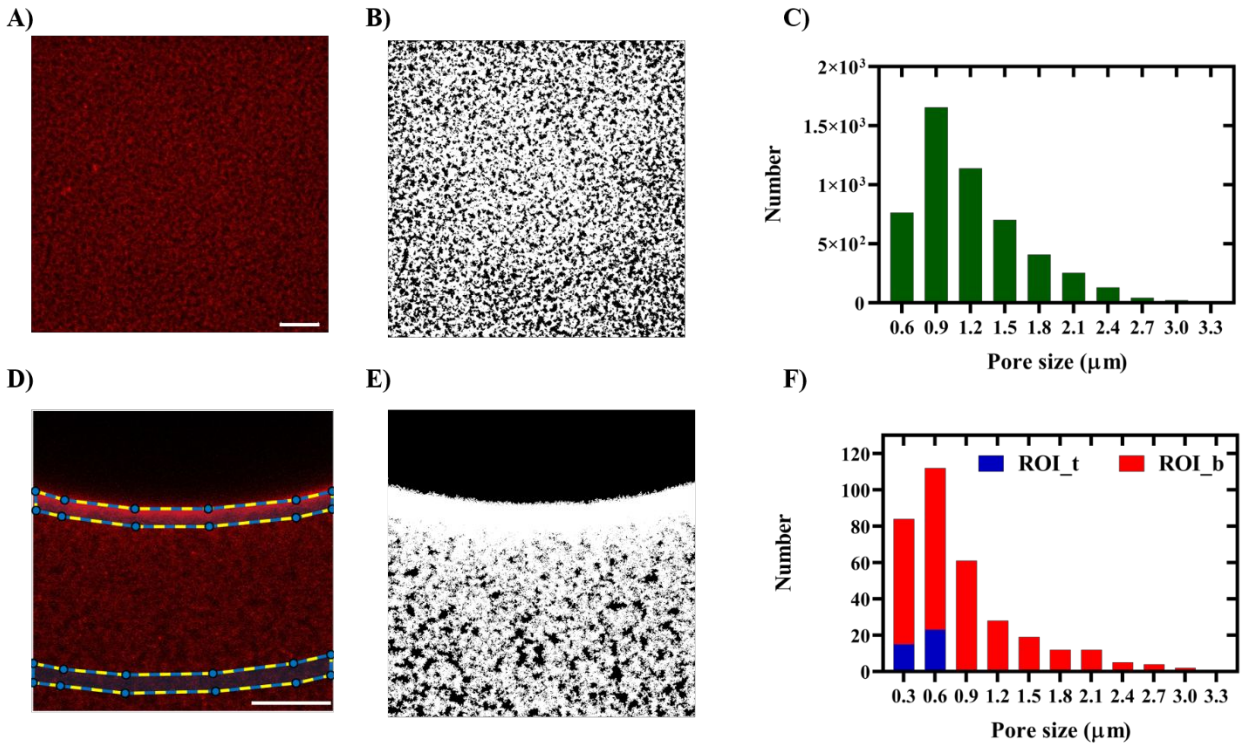

Figure 5. The fibrin matrix and pore size distribution were impacted by a bubble generated via acoustic droplet vaporization (ADV). 2D confocal images (79.5 μm by 79.5 μm) of a fibrin-only gel (A) and an acoustically-responsive scaffold (ARS) 24 hours post-ADV (D). The corresponding binary images are shown in (B) and (E), respectively. The pore size distribution of fibrin-only gels (C) and an ARS (F) is presented. The top and bottom regions of interest (ROIs), each having a length of 10 μm, were chosen in (D) to calculate and compare pore size distribution in regions proximal and distal from the bubble-fibrin interface. (F) Representative pore size distribution of top ROI (ROI_t) and bottom ROI (ROI_b) calculated using image processing functions in MATLAB. Scale bar: 20 μm.

In our previous publication, we showed that ADV reduced the rate of fibrin degradation, either as a result of hindered diffusivity or increased stiffness through bulk measurements [13]. In this study, we confirmed ADV-induced changes in the microstructure of the fibrin matrix, such as locally increased fibrin density and reduced pore size distribution, through time dependent confocal imaging. Considerable previous work has documented significance of mechanical (e.g., elasticity) and microstructural (e.g., pore size, fiber density) properties of the local microenvironment on cellular behaviors such as spreading, directional migration, and

differentiation [47-49]. This suggests that ADV can be used as a tool to spatiotemporally tune the kinetics of payload release (i.e., faster or slower release), degradation kinetics, directional migration of cells, and regenerative processes in hydrogels [13, 14].

3.1.2 Morphology of ADV-generated bubbles in ARSs

Depending on the vertical distance (L) of the PSDE with respect to the bottom of the well (i.e., silicone elastomer, see Fig. 1(D)), different bubble responses were observed in ARSs post ADV. Since the excitation pressure (P_r = 8 MPa) was above the IC threshold (3.9 ± 0.2 MPa), the ADV-generated bubbles could collapse inside the ARS at or near the ARS-silicone elastomer boundary. Figure 6 summarizes different bubble behaviors observed in ARSs using confocal imaging. Spherical ADV-generated bubbles (Figs. 6(A) and (B)) were observed through the bulk of the gel (L > ~300 μm). Morphology of bubbles in a viscoelastic medium depends on the interfacial tension and the surrounding medium rheology [50]. Mougin et al. showed that during expansion, bubbles were more distorted (i.e., elongated) in a medium of high viscosity while remained spherical in low viscosity fluids [51]. Since fibrin gels used in this study had similar bulk modulus to that of water, as shown previously by measuring the speed of sound in fibrin (1497± 3.6 m/s) [24] and water (1483 m/s) [52], more spherical shapes are expected for ADV-generated bubbles within fibrin gels. In gels of higher bulk modulus, non-circular bubbles were observed 3 days post-ADV [53].

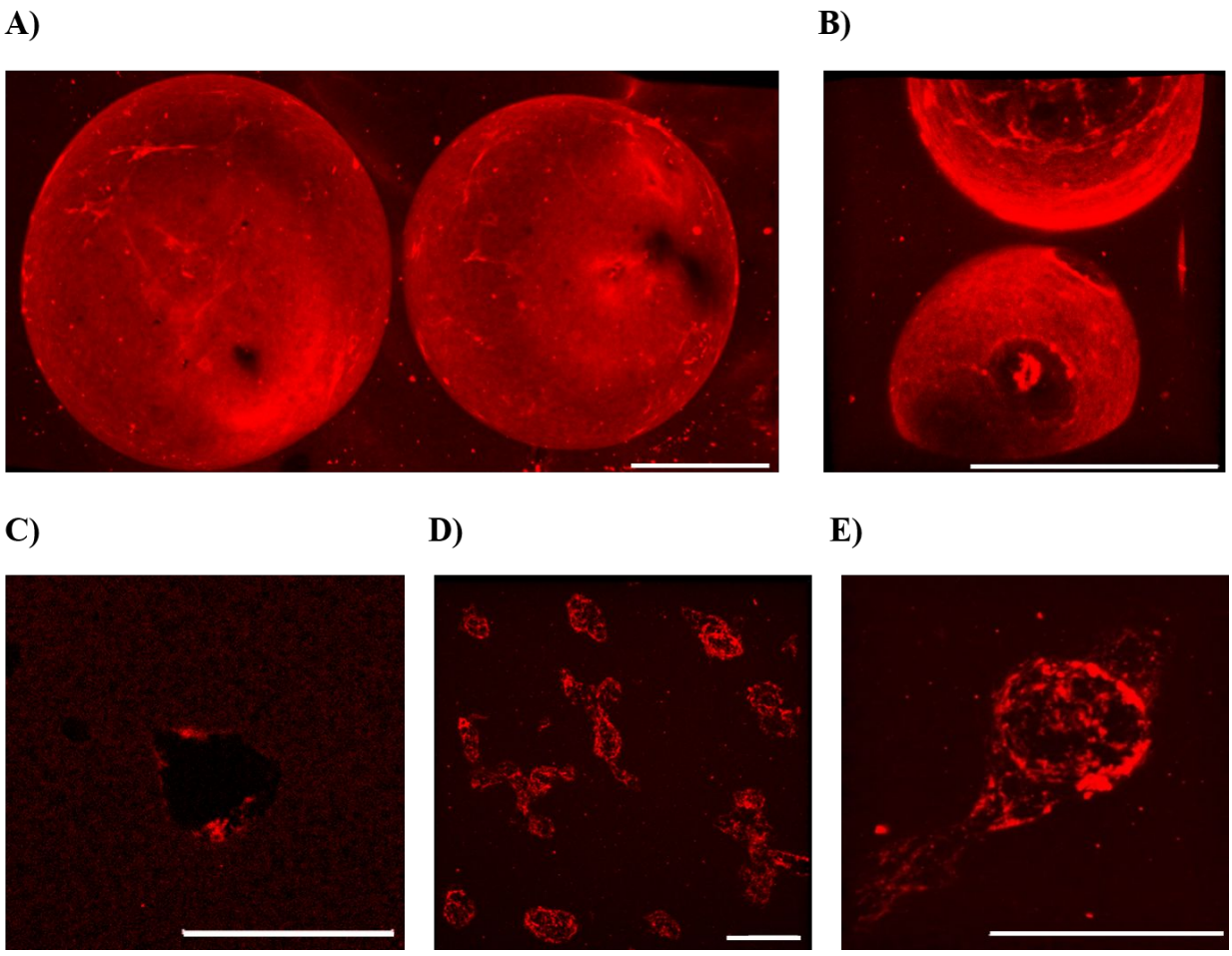

Figure 6. Confocal images demonstrating bubble morphologies generated via acoustic droplet vaporization (ADV) in acoustically-responsive scaffolds (ARSs). ADV generated different features depending on the vertical distance from the bottom of fluorescently-labeled ARSs containing 0.005 % (v/v) perfluorohexane double emulsion. (A) and (B) maximum intensity projection confocal images of ADV-generated spherical bubbles. (C) 2D, (D) and (E) maximum intensity projection confocal images of asymmetrically collapsed features. ARSs were imaged 1-hour post ADV. Scale bar: 50μm.

Visual indications of possible asymmetrically collapsed ADV-generated bubbles were observed at L< ~300 μm (Fig. 6 (C)-(E)). The proximity of the solid boundary affects the dynamic response of bubbles in an US field. Interactions between a cavitating bubble and a nearby boundary can induce microjetting, where the direction of jetting can be toward (rigid boundaries) or away from (soft boundaries) the boundary, depending on the mechanical properties of the boundary,

bubble size (R), and L [54-56]. Microjet formation has been observed experimentally [57] and numerically [58] at nondimensional standoff parameter (L/R) ranging from 0.5-3. Larger standoff distances would cause the bubble to oscillate more cycles before collapsing. Jetting toward or away from an elastic wall was numerically observed at density ratios ($\rho_{wall}/\rho_{medium}$) greater and less than 1.4, respectively [58]. In this study an excitation pressure of 8 MPa (P_r) was chosen since it resulted in a higher ADV efficiency as shown in our prior publications [13, 14]. Acoustic parameters such as excitation frequency, pulse duration, and the driving amplitude would likely impact both the dynamics and resulting morphologies of the ADV-generated features. For a sufficiently sized bubble, the number of cycles required for microjet formation decreased with the driving amplitude. For a driving pressure beyond a threshold, microjets were produced in the first collapse cycle [57]. Microjet formation was also dependent on the ratio of the excitation frequency and the resonance frequency of the bubble [59]. Given the size of the ADV-generated bubbles in our study, microjet formation may only be observed at low MHz frequencies. As will be discussed in the following section, the probability of microjet formation increases as the inter-bubble distance decreases, depending on the size and the phase difference of the oscillating bubbles [60, 61]. Therefore, higher volume fractions of ADV-generated bubbles may result in higher fluid-filled macropore formation. In addition to ADV-generated asymmetrically-collapsed bubbles, the size of the ADV-generated stable bubbles inversely and directly correlate with the frequency of excitation and pulse duration, respectively [62]. A systematic investigation is required to examine the effects of acoustic parameters (as listed above), physical parameters (i.e., size and surface tension of PFC emulsion), and bulk medium rheology (i.e., elasticity of the hydrogel matrix) on the ADV-generated features.

3.1.3 Growth dynamics of ADV-generated features in ARSs

The growth of ADV-generated, spherical bubbles in ARSs was longitudinally monitored using confocal imaging (10x). Assuming complete vaporization of the PFC phase and neglecting in-gassing during ADV, a ~6.3 μm PSDE (containing 67% (v/v) PFH) is expected to yield a ~20 μm bubble [63]. Figures 7(A) & (B) show maximum intensity projections of confocal z-stacks of ARSs 1h and 3d post ADV, respectively.The radius of the spherical bubble in the equilibrium state (i.e., post US) increased due to transfer of dissolved gases (i.e., air) in the medium (i.e., fibrin) across the interface. The average radii of ADV-generated bubbles reached 32.8 ± 9.2 μm (1h), 61.6 ± 21.4 μm (2d), 75.5 ± 37.5 μm (3d), and 88.5 μm [86.0, 105.2] (4d). Bubble size significantly increased over the time points studied here, resulting in a growth rate of ~31 μm/day (Fig. 7(C)) in diameter. The expansion ratios, with respect to the initial size of the PSDE (∅ ~6.3 μm), were ~4 (1h), ~11(1d), ~21 (2d), ~26 (3d), and ~32 (4d). For a single lipid-coated PFC emulsion an expansion factor of ~15 was reported within 15 minutes post ADV in water through optical observations [64]. Bubble growth is determined by several parameters such as shell permeability, surface tension, gas saturation, diffusivity of the inner gas, and the bubble volume fraction. For PFCs, particularly with increasing carbon chain length such as PFH, the coefficients of diffusivity, solubility, and permeability are significantly lower (orders of magnitude) than air, making it favorable for the inward diffusion of air [65, 66]. Note that permeability decreases significantly as the encapsulation thickness increases. Furthermore, Borden et al. showed that the shell-induced resistance to gas transfer, rather than Laplace pressure, played the dominant role in bubble size evolution [67]. The ADV-generated bubbles in ARSs, irrespective of whether the initial Pluronic shell was partially or completely retained, were surrounded by an extra layer of highly dense fibrin (Fig. 2(B)) with a FWHM thickness in the micrometer range (see Fig. 4), resulting in superstable

bubbles. In addition to hindered permeability due to encapsulation, the large size of these ADV-generated bubbles (i.e., lower surface tension) increased their lifetime. Sarkar et al. showed that an increase from 2 to 20 µm in bubble radius increased the dissolution time by a hundred [65].

Static diffusion governed the growth of these super-shelled, ADV-generated bubbles in ARSs. As shown in Fig. 7 (C), the bubble's initial growth was faster since it was controlled by the initial partial pressure of air and PFH vapor and the resulting pressure gradient [68]. Note that other mechanisms such as coalescence or Ostwald ripening can influence the growth as well [69].

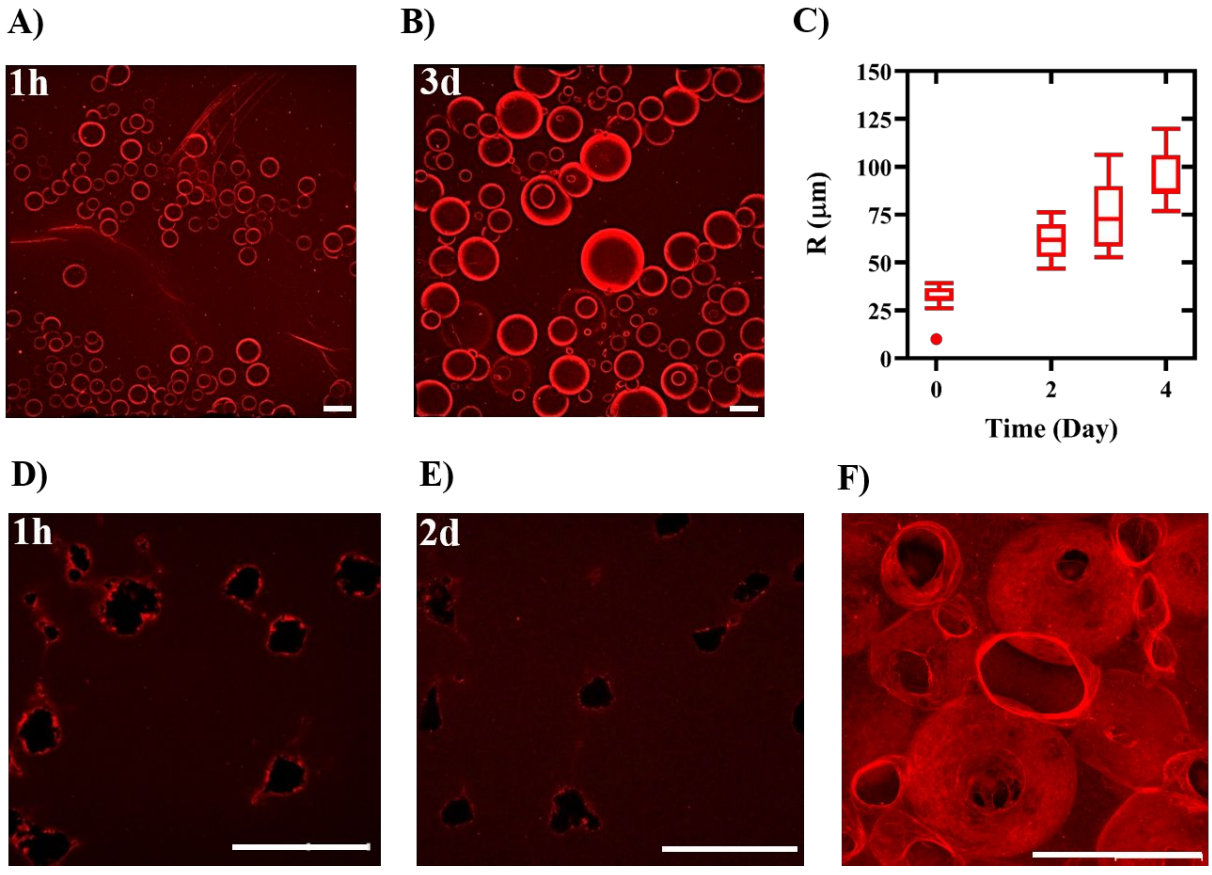

Figure 7. Comparison of the growth dynamics of gas-filled and fluid-filled features generated in acoustically-responsive scaffolds (ARSs) post acoustic droplet vaporization (ADV). Maximum intensity projection of confocal images (1.28 mm by 1.28 mm) of ARSs containing 0.005% (v/v) perfluorohexane emulsion (A) 1-hour (1h) and (B) 3 days (3d) post ADV. (C) Temporal evolution of the radius (R) of the ADV-generated bubbles measured from confocal images (N=25). ADV-generated fluid-filled macropores, resulting from acoustically-driven microjetting, after (D) 1h, and (E) 2d post-ADV showed no significant

change in size. Maximum intensity projection of an ARS with a higher volume fraction (1% (v/v) of phase-shift double emulsion at 1h is shown in (F). Scale bar: 100 μm.

Contrary to the growth of spherical bubbles, no significant change in the size of the asymmetrically collapsed features was observed (Fig. 7(D) & (E)), indicating a gas-free macropore. To further examine the gas and fluid content of the ADV-generated features, ARSs (post-ADV) were exposed to an overpressure of ~35 kPa for one minute and then imaged (Fig. S2). The asymmetrically collapsed features showed no significant change in size under static compression while spherical bubbles were collapsed. The relative lack of change in the conformations of structures after compression is consistent with the suggested mechanism of microjetting. This demonstrates that ADV can generate stable bubbles as well as macropores, void of gas possibly as a result of microjetting, within the hydrogel matrix in a spatiotemporal manner. Presence of stable bubbles can be used to tune kinetics of degradation as well as payload release as shown in our previous studies [13, 70]. The ability to spatiotemporally control macropore generation in hydrogels *in situ* is desirable for many biomedical applications. One particular application of macropores can be in tissue regeneration where a direct correlation between micro-cavity density and vascularization has been reported [71].

Note that in this study, a lower volume fraction of emulsion (0.005%) was chosen to facilitate studies of isolated ADV-generated bubbles. We showed bubble-boundary interactions yielded fluid-filled macropores. Apart from the presence of a solid boundary, parameters such as size and inter-bubble distance and oscillation period can determine the morphology of collapse. Jetting can also be observed between two oscillating bubbles depending on their separation distance and phase difference [60, 61]. Increasing the volume fraction would enhance the probability of bubble-bubble interactions. Figure 7(F) illustrates the confocal image of an ARS with 1% (v/v) PSDE 1h post

ADV. This approach could be used to generate ADV-induced interconnected macropores within ARSs, which is currently under investigation.

3.2 AFM mechanical characterization

AFM revealed the micromechanical heterogeneity of ARSs post ADV, on the scale of the probe size. A typical F-d curve from an ARS post ADV is displayed in Fig. 8(A). The assumption of a linear relationship between stress and stain is valid for small deformations, as can be seen. To further assess the reproducibility of AFM measurements as well as the linear elastic assumption of the Hertz theory, f-δ curves were obtained from the same location across consecutive loading and unloading cycles. Representative sequential compression curves on fibrin-only gels (Fig. S3(A)), ARSs (-US) (Fig. 8(B)), and ARSs (+US) (Fig. S3(B)) indicate that the samples were successfully immobilized during the measurements and also restored their original shape after repeated loading and unloading cycles (i.e., no plastic deformation). Young's moduli (Fig. 8(C)) were 0.47 ± 0.07 kPa and 0.23 ± 0.08 kPa for fibrin-only gels and ARSs containing 1% (v/v) PSDEs (-US), respectively. Note that compressibility (κ) of a medium is inversely proportional to the square of speed of sound in that medium. PFC liquids are more compressible ($\kappa \sim 2.02 \times 10^{-9}$ m•s^2/kg) than fibrin ($\kappa \sim 4.45 \times 10^{-10}$ m•s^2/kg) due to their low speed of sound (~500 m/s), resulting in a lower Young's modulus in ARSs (-US) [11, 72].

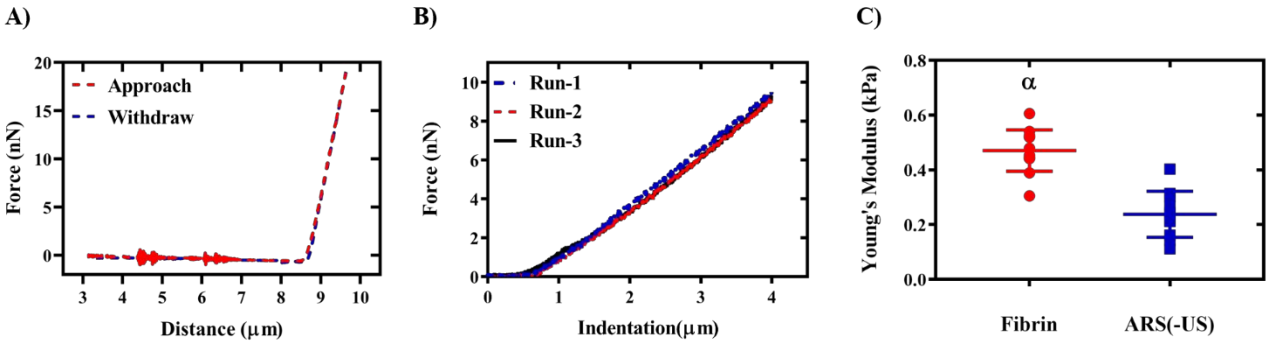

Figure 8. Atomic force microscopy (AFM) was used to measure micromechanical properties of acoustically-responsive scaffolds (ARS) before and after acoustic droplet vaporization (ADV). (A) A typical force-distance curve for an ARS post ADV. Force-distance curves were converted to force-indentation following Hooke's Law. The compression curve (i.e., approach) was used to calculate Young's modulus according to the Hertz model. (B) Repeated compression curves on the same location in an ARS(-US) resulted in no permanent deformation, demonstrating the linear elastic regime. (C) The average Young's moduli of fibrin-only gels and ARSs, containing 1% (v/v) perfluorohexane double emulsion, were 0.47 ± 0.07 kPa and 0.23 ± 0.08 kPa, respectively. Statistically significant difference ($p < 0.05$) is denoted as follows: α: vs. ARS(-US).

For time-dependent micromechanical properties of ARSs containing 0.005% (v/v) PSDEs post-ADV, two regions with and without bubbles (denoted as 3 and 2, respectively, in Fig. 9(A)) were chosen based on optical microscopy. The measured Young's modulus increased significantly (~70%) in the ADV-generated bubble region (1.6 ± 0.6 kPa) compared to the non-bubble region (0.46 [0.27, 0.51] kPa) 1h post ADV as shown in Fig. 9(B). This figure also displays the span of Young's moduli in the non-bubble region which is similar to the fibrin-only gel and ARSs (-US) cases (Fig. 8(C)). The time-dependent Young's moduli for the bubble region were 2.1 ± 1.2 kPa (1h), 2.2 ± 1.6 kPa (1d), 6.4 ± 3.5 kPa (2d), and 8.9 ± 4.4 kPa (4d). Similarly, for the non-bubble region, Young's moduli were 0.41 [0.27, 0.51] kPa (1h), 0.39 ± 0.11 kPa (1d), 0.41 ± 0.16 kPa (2d), and 0.44 [0.27, 0.58] kPa (4d). The relatively large variability in Young's modulus of the bubble region in ARSs stems from the difference in distances of the ADV-generated bubbles from

the surface. Due to objective magnification and working distance restrictions, it was not possible to evaluate the depth of the bubbles.

Additionally, the longitudinal increase in Young's modulus in the bubble-region agrees with the increase in FWHM thickness of the high intensity region surrounding the ADV bubbles shown in Fig. 3(B). Note that several groups reported much higher and size-dependent stiffnesses (in the N/m range) and Young's moduli (in the MPa range) through direct AFM measurements on contrast microbubbles [27, 73]. Here, the measured values reflect the micromechanical properties of fibrin in the vicinity of ADV-bubbles and PSDEs. This also has been confirmed by confocal images from the surface of the ARSs (Fig. S4). In addition, using Stokes' law, the terminal velocity of PSDEs (density: 1400 kg/m^3, average diameter: 6.3 μm) was ~ 3 μm/s. Assuming a polymerization time of 10 s, before viscosity increased significantly, PSDEs would settle ~30 μm below the top surface.

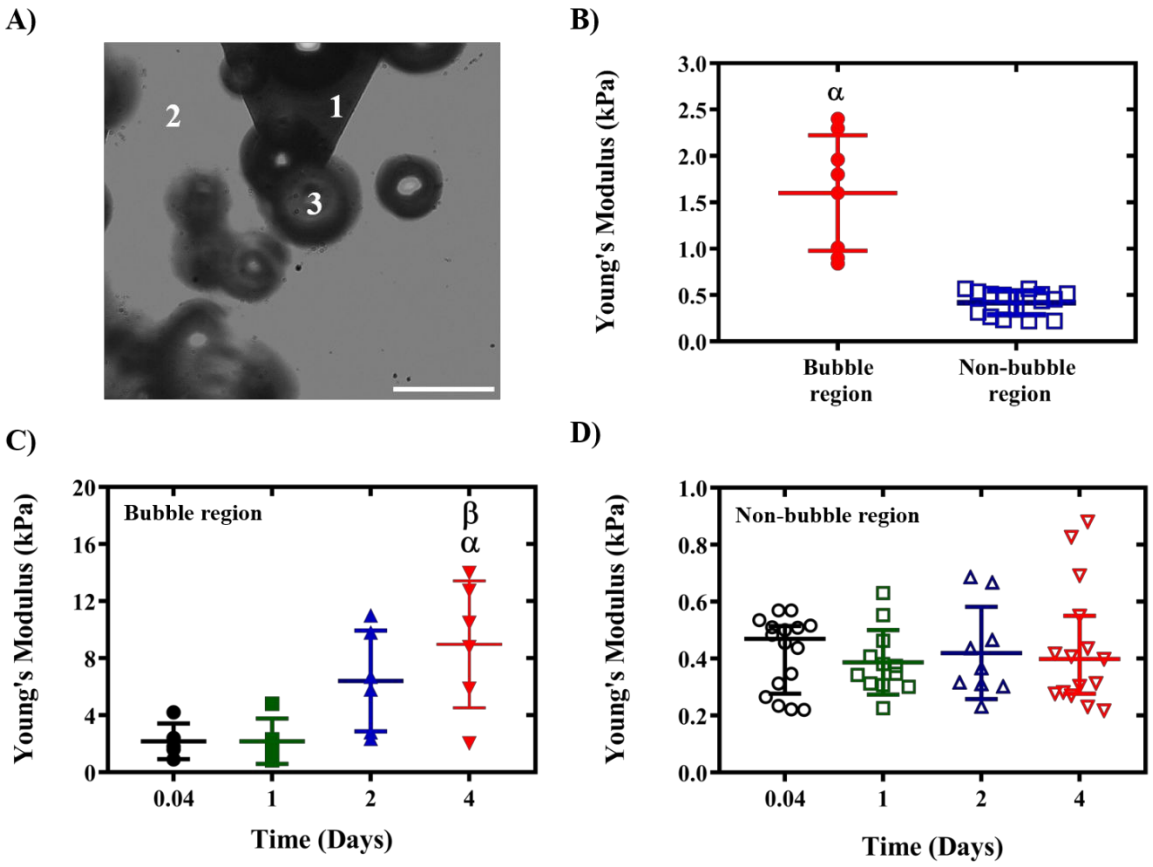

Figure 9. Atomic force microscopy (AFM) was used to investigate the time-dependent micromechanical properties of acoustically-responsive scaffolds (ARSs) post acoustic droplet vaporization (ADV). The AFM was mounted on an inverted optical microscope. (A) An optical image of an ARS 1-hour (1h) post ADV shows the cantilever (1), non-bubble (2) and bubble (3) regions. (B) Calculated Young's moduli, based on the Hertz theory, of bubble and non-bubble regions of an ARS 1h post ADV. Summary of calculated Young's moduli on (C) the bubble and (D) non-bubble regions of ARSs as a function of time. Statistically significant differences ($p < 0.05$) are denoted as follows: α: vs. Non-bubble region in (B), and α: vs. 1h; β: vs. 1d in (C). Scale bar: 100 μm.

The ADV-induced, local increase in the elastic moduli of ARSs - 5.2-fold (1h), 5.7-fold (1d), 15.6-fold (2d), and 20.4-fold (4d) compared to the non-bubble regions at the same timepoint - was consistent with strain-induced stiffening of fibrin gels [74]. Storm et al. reported a 10-fold increase in the shear modulus of fibrin under strains as small as 20% [75]. Note that we previously reported a 300% increase in shear stiffness for an ARS containing 1% (v/v)

perfluoropentane emulsion post-ADV compared to sham-treated ARSs, using dynamic shear testing [12]. On a microscale level, cell-induced stiffening resulted in a 3-fold increase in the elastic modulus of fibrin gels [46].

Since fibrin has a complex, hierarchical structure (i.e., fibers, protofibrils, and monomers), different stress-response mechanisms are proposed depending on the amount of strain. However, strain stiffening, characteristic of semiflexible filamentous networks, mainly stems either from the nonlinear elasticity of single filaments (entropic model) resisting extension, or alignment of fibers in the direction of strain (nonentropic model) [35, 76].

Cells sense and respond to the micromechanics of their surroundings [77, 78]. Increased substrate as well as fiber elasticity significantly altered cell spreading, proliferation, and differentiation [79-81]. ADV-induced stiffness in ARSs both on a microscale, which was investigated here, and a bulk level, which was previously shown [12], can allow design of scaffolds with tunable mechanics in a spatiotemporally-controlled manner.

4 Conclusions

We have studied time-dependent, micromechanical and microstructural properties of ARSs post-ADV through confocal imaging and AFM. As a result of ADV-induced mechanical strain, localized restructuring of fibrin occurred at the bubble-fibrin interface, forming locally denser regions. The intensity as well as the FWHM of this region increased significantly over time, indicating a correlation between fibrin compaction and bubble growth. Additionally, the presence of an ADV-generated bubble significantly reduced both size and number of pores in the surrounding matrix compared to a fibrin-only gels. Furthermore, ADV-generated features with gas or liquid contents displayed distinct morphologies and were observed to be spatially-dependent

within the ARSs. The gas-filled cavities grew due to mass transfer of the dissolved gases in their surroundings, while the size of the fluid-filled ones did not change significantly. AFM measurements confirmed ADV-induced stiffening of an ARS in the vicinity of an ADV-generated bubble. These findings highlight the ability of ADV to non-invasively modulate matrix mechanics and macrostructures in ARSs in an on-demand, spatiotemporally manner, which can be used for future regenerative applications.

Conflicts of interest

There are no conflicts to declare.

Acknowledgments

This work was supported by NIH Grant R01HL139656 (M.L.F.) and R00HL124322 (B.M.B). C.D.D. acknowledges financial support from the National Science Foundation Graduate Research Fellowship Program (DGE1256260). W.Y.W. acknowledges financial support from the University of Michigan Rackham Merit Fellowship and the National Science Foundation Graduate Research Fellowship Program (DGE1256260). Special thanks to Dr. Allen Brooks (Department of Radiology) for assisting with the synthesis of the fluorosurfactant, Edwin De Feijter and Dr. Miles J McKenna for helpful discussions on confocal microscopy, the Fabrication Studio at the Duderstadt Center and Dr. William Weadock (Department of Radiology) for helping with 3D printing of materials related to the US exposure setup.

5 References

1. W. L. Murphy, T. C. McDevitt and A. J. Engler, *Nat Mater*, 2014, **13**, 547-557.
2. G. ter Haar, *Prog Biophys Mol Biol*, 2007, **93**, 111-129.
3. D. Dalecki, *Annu Rev Biomed Eng*, 2004, **6**, 229-248.
4. O. D. Kripfgans, J. B. Fowlkes, D. L. Miller, O. P. Eldevik and P. L. Carson, *Ultrasound Med Biol*, 2000, **26**, 1177-1189.
5. O. D. Kripfgans, C. M. Orifici, P. L. Carson, K. A. Ives, O. P. Eldevik, J. B. J. I. t. o. u. Fowlkes, ferroelectrics, and f. control, 2005, **52**, 1101-1110.
6. P. S. Sheeran, S. H. Luois, L. B. Mullin, T. O. Matsunaga and P. A. Dayton, *Biomaterials*, 2012, **33**, 3262-3269.
7. A. Qamar, Z. Z. Wong, J. B. Fowlkes and J. L. Bull, *Appl Phys Lett*, 2010, **96**, 143702.
8. J. E. Chomas, P. Dayton, J. Allen, K. Morgan and K. W. Ferrara, *IEEE Trans Ultrason Ferroelectr Freq Control*, 2001, **48**, 232-248.
9. W. Lauterborn and T. Kurz, *Reports on Progress in Physics*, 2010, **73**, 106501.
10. M. L. Fabiilli, K. J. Haworth, N. H. Fakhri, O. D. Kripfgans, P. L. Carson and J. B. Fowlkes, *IEEE Trans Ultrason Ferroelectr Freq Control*, 2009, **56**, 1006-1017.
11. M. Aliabouzar, K. N. Kumar and K. Sarkar, *J Acoust Soc Am*, 2019, **145**, 1105.
12. M. L. Fabiilli, C. G. Wilson, F. Padilla, F. M. Martín-Saavedra, J. B. Fowlkes and R. T. Franceschi, *Acta biomaterialia*, 2013, **9**, 7399-7409.
13. M. Aliabouzar, A. Jivani, X. Lu, O. D. Kripfgans, J. B. Fowlkes and M. L. Fabiilli, *Ultrason Sonochem*, 2020, **66**, 105109.
14. X. Lu, X. Dong, S. Natla, O. D. Kripfgans, J. B. Fowlkes, X. Wang, R. Franceschi, A. J. Putnam and M. L. Fabiilli, *Ultrasound Med Biol*, 2019, **45**, 2471-2484.
15. A. Moncion, M. Lin, E. G. O'Neill, R. T. Franceschi, O. D. Kripfgans, A. J. Putnam and M. L. Fabiilli, *Biomaterials*, 2017, **140**, 26-36.
16. M. L. Fabiilli, J. A. Lee, O. D. Kripfgans, P. L. Carson and J. B. Fowlkes, *Pharm Res*, 2010, **27**, 2753-2765.
17. X. Dong, X. Lu, K. Kingston, E. Brewer, B. A. Juliar, O. D. Kripfgans, J. B. Fowlkes, R. T. Franceschi, A. J. Putnam, Z. Liu and M. L. Fabiilli, *Acta Biomater*, 2019, **97**, 409-419.
18. R. Asami, T. Ikeda, T. Azuma, S. Umemura and K.-i. Kawabata, *Japanese Journal of Applied Physics*, 2010, **49**, 07HF16.

19. R. Williams, C. Wright, E. Cherin, N. Reznik, M. Lee, I. Gorelikov, F. S. Foster, N. Matsuura and P. N. Burns, *Ultrasound Med Biol*, 2013, **39**, 475-489.
20. C. L. Chiu, V. Hecht, H. Duong, B. Wu and B. Tawil, *Biores Open Access*, 2012, **1**, 34-40.
21. J. E. Parsons, C. A. Cain and J. B. Fowlkes, *J Acoust Soc Am*, 2006, **119**, 1432-1440.
22. M. P. Burke, J. D. Smith, N. L. Carroll, D. J. Townend, D. Porter and P. R. Hoskins, *Plastics, Rubber and Composites*, 2013, **38**, 343-348.
23. K. A. Garvin, D. C. Hocking and D. Dalecki, *Ultrasound Med Biol*, 2010, **36**, 1919-1932.
24. M. Aliabouzar, X. Lu, O. D. Kripfgans, J. B. Fowlkes and M. L. Fabiilli, *Ultrasound Med Biol*, 2019, **45**, 3246-3260.
25. A. Rabbani, S. Jamshidi and S. Salehi, *Journal of Petroleum Science and Engineering*, 2014, **123**, 164-171.
26. L. Shapiro, *Computer vision and image processing*, Academic Press, 1992.
27. C. C. Chen, S. Y. Wu, J. D. Finan, B. Morrison, 3rd and E. E. Konofagou, *IEEE Trans Ultrason Ferroelectr Freq Control*, 2013, **60**, 524-534.
28. V. Sboros, E. Glynos, S. D. Pye, C. M. Moran, M. Butler, J. Ross, R. Short, W. N. McDicken and V. Koutsos, *Ultrasound Med Biol*, 2006, **32**, 579-585.
29. Y. M. Efremov, T. Okajima and A. Raman, *Soft Matter*, 2020, **16**, 64-81.
30. C. D. Markert, X. Guo, A. Skardal, Z. Wang, S. Bharadwaj, Y. Zhang, K. Bonin and M. Guthold, *J Mech Behav Biomed Mater*, 2013, **27**, 115-127.
31. K. D. Costa, *Dis Markers*, 2003, **19**, 139-154.
32. S. W. Moore, P. Roca-Cusachs and M. P. Sheetz, *Dev Cell*, 2010, **19**, 194-206.
33. B. Dollet, P. Marmottant and V. Garbin, *Annual Review of Fluid Mechanics*, 2019, **51**, 331-355.
34. T. Hayashi, M. Hasegawa, J. Inamasu, K. Adachi, S. Nagahisa and Y. Hirose, *Neurol Med Chir (Tokyo)*, 2014, **54**, 895-900.
35. S. Nam, K. H. Hu, M. J. Butte and O. Chaudhuri, *Proc Natl Acad Sci U S A*, 2016, **113**, 5492-5497.
36. C. M. Ghajar, X. Chen, J. W. Harris, V. Suresh, C. C. Hughes, N. L. Jeon, A. J. Putnam and S. C. George, *Biophys J*, 2008, **94**, 1930-1941.
37. O. Moreno-Arotzena, J. G. Meier, C. Del Amo and J. M. Garcia-Aznar, *Materials (Basel)*, 2015, **8**, 1636-1651.
38. N. E. Hudson, J. R. Houser, E. T. O'Brien, 3rd, R. M. Taylor, 2nd, R. Superfine, S. T. Lord and M. R. Falvo, *Biophys J*, 2010, **98**, 1632-1640.
39. Q. Wen, A. Basu, J. P. Winer, A. Yodh and P. A Janmey, *New Journal of Physics*, 2007, **9**, 428-428.

40. O. V. Kim, R. I. Litvinov, J. W. Weisel and M. S. Alber, *Biomaterials*, 2014, **35**, 6739-6749.
41. W. Liu, C. R. Carlisle, E. A. Sparks and M. Guthold, *J Thromb Haemost*, 2010, **8**, 1030-1036.
42. J. Song, M. Caggioni, T. M. Squires, J. F. Gilchrist, S. W. Prescott and P. T. Spicer, *Rheologica Acta*, 2019, **58**, 217-229.
43. J. P. Winer, S. Oake and P. A. Janmey, *PLoS One*, 2009, **4**, e6382.
44. N. R. Lang, K. Skodzek, S. Hurst, A. Mainka, J. Steinwachs, J. Schneider, K. E. Aifantis and B. Fabry, *Acta Biomater*, 2015, **13**, 61-67.
45. B. A. Harley, T. M. Freyman, M. Q. Wong and L. J. Gibson, *Biophys J*, 2007, **93**, 2911-2922.
46. K. A. Jansen, R. G. Bacabac, I. K. Piechocka and G. H. Koenderink, *Biophys J*, 2013, **105**, 2240-2251.
47. C. Cha, J. H. Jeong, J. Shim and H. Kong, *Acta Biomater*, 2011, **7**, 3719-3728.
48. M. P. Lutolf, J. L. Lauer-Fields, H. G. Schmoekel, A. T. Metters, F. E. Weber, G. B. Fields and J. A. Hubbell, *Proc Natl Acad Sci U S A*, 2003, **100**, 5413-5418.
49. D. L. Matera, W. Y. Wang, M. R. Smith, A. Shikanov and B. M. Baker, *ACS Biomaterials Science & Engineering*, 2019, **5**, 2965-2975.
50. R. Clift, J. R. Grace and M. E. Weber, *Bubbles, drops, and particles*, Courier Corporation, 2005.
51. N. Mougin, A. Magnin and J.-M. Piau, *Journal of Non-Newtonian Fluid Mechanics*, 2012, **171**, 42-55.
52. F. A. Duck, *Physical properties of tissues: a comprehensive reference book*, Academic press, 2013.
53. C. M. Carneal, O. D. Kripfgans, J. Krucker, P. L. Carson and J. B. Fowlkes, *IEEE Trans Ultrason Ferroelectr Freq Control*, 2011, **58**, 2013-2025.
54. H. Chen, A. A. Brayman, W. Kreider, M. R. Bailey and T. J. Matula, *Ultrasound Med Biol*, 2011, **37**, 2139-2148.
55. W. Lauterborn and H. Bolle, *Journal of Fluid Mechanics*, 2006, **72**, 391-399.
56. E.-A. Brujan, K. Nahen, P. Schmidt and A. Vogel, *Journal of Fluid Mechanics*, 2001, **433**, 283-314.
57. J. M. Rosselló, W. Lauterborn, M. Koch, T. Wilken, T. Kurz and R. Mettin, *Physics of Fluids*, 2018, **30**, 122004.
58. S. W. Ohl, E. Klaseboer and B. C. Khoo, *Phys Med Biol*, 2009, **54**, 6313-6336.
59. E. A. Brujan, *Ultrasound Med Biol*, 2004, **30**, 381-387.

60. L. W. Chew, E. Klaseboer, S. W. Ohl and B. C. Khoo, *Phys Rev E Stat Nonlin Soft Matter Phys*, 2011, **84**, 066307.
61. T. Hopfes, Z. Wang, M. Giglmaier and N. A. Adams, *Experimental Thermal and Fluid Science*, 2019, **108**, 104-114.
62. T. Leighton, *The acoustic bubble*, Academic press, 2012.
63. O. D. Kripfgans, C. M. Orifici, P. L. Carson, K. A. Ives, O. P. Eldevik and J. B. Fowlkes, *IEEE Trans Ultrason Ferroelectr Freq Control*, 2005, **52**, 1101-1110.
64. N. Reznik, M. Seo, R. Williams, E. Bolewska-Pedyczak, M. Lee, N. Matsuura, J. Gariepy, F. S. Foster and P. N. Burns, *Phys Med Biol*, 2012, **57**, 7205-7217.
65. K. Sarkar, A. Katiyar and P. Jain, *Ultrasound Med Biol*, 2009, **35**, 1385-1396.
66. A. S. Kabalnov, K. N. Makarov, O. V. Shcherbakova and A. N. Nesmeyanov, *Journal of Fluorine Chemistry*, 1990, **50**, 271-284.
67. M. A. Borden and M. L. Longo, *Langmuir*, 2002, **18**, 9225-9233.
68. K. P. Mercado-Shekhar, H. Su, D. S. Kalaikadal, J. N. Lorenz, R. M. Manglik, C. K. Holland, A. N. Redington and K. J. Haworth, *Ultrason Sonochem*, 2019, **56**, 114-124.
69. J. Schmelzer and F. Schweitzer, *Journal of Non-Equilibrium Thermodynamics*, 1987, **12**, 255-270.
70. X. Lu, X. Dong, S. Natla, O. D. Kripfgans, J. B. Fowlkes, X. Wang, R. Franceschi, A. J. Putnam, M. L. J. U. i. M. Fabiilli and Biology, 2019, **45**, 2471-2484.
71. J. Fu, C. Fan, W. S. Lai and D. Wang, *Biomed Mater*, 2016, **11**, 055012.
72. E. M. Strohm and M. C. Kolios, 2011.
73. V. Sboros, E. Glynos, S. Pye, C. Moran, M. Butler, J. Ross, W. McDicken and V. J. U. Koutsos, 2007, **46**, 349-354.
74. I. Levental, P. C. Georges and P. A. Janmey, *Soft Matter*, 2007, **3**, 299-306.
75. C. Storm, J. J. Pastore, F. C. MacKintosh, T. C. Lubensky and P. A. J. N. Janmey, 2005, **435**, 191-194.
76. I. K. Piechocka, R. G. Bacabac, M. Potters, F. C. Mackintosh and G. H. Koenderink, *Biophys J*, 2010, **98**, 2281-2289.
77. R. J. Petrie, N. Gavara, R. S. Chadwick and K. M. Yamada, *J Cell Biol*, 2012, **197**, 439-455.
78. O. Chaudhuri, L. Gu, D. Klumpers, M. Darnell, S. A. Bencherif, J. C. Weaver, N. Huebsch, H. P. Lee, E. Lippens, G. N. Duda and D. J. Mooney, *Nat Mater*, 2016, **15**, 326-334.

79. N. D. Evans, C. Minelli, E. Gentleman, V. LaPointe, S. N. Patankar, M. Kallivretaki, X. Chen, C. J. Roberts and M. M. Stevens, *Eur Cell Mater*, 2009, **18**, 1-13; discussion 13-14.
80. B. M. Baker, B. Trappmann, W. Y. Wang, M. S. Sakar, I. L. Kim, V. B. Shenoy, J. A. Burdick and C. S. Chen, *Nat Mater*, 2015, **14**, 1262-1268.
81. W. Y. Wang, C. D. Davidson, D. Lin and B. M. Baker, *Nat Commun*, 2019, **10**, 1186.

Acoustic droplet vaporization (ADV) of phase shift emulsion (green) generates different bubble morphologies, and spatiotemporally tunes the micromechanics of fibrin gels (red).